HHS Public Access

Author manuscript

Mitochondrion. Author manuscript; available in PMC 2024 September 12.

Published in final edited form as:

Mitochondrion. 2024 September ; 78: 101933. doi:10.1016/j.mito.2024.101933.

Differentiation activates mitochondrial OPA1 processing in myoblast cell lines

Harpreet Kaur[a,*], **Omar Carrillo**[a,*], **Iraselia Garcia**[a,c], **Isaiah Ramos**[a], **Shaynah St. Vallier**[a], **Patrick De La Torre**[a], **Alma Lopez**[a], **Megan Keniry**[a], **Daniel Bazan**[a], **Jorge Elizondo**[a], **Grishma KC**[d], **Lee Ann MacMillan-Crow**[d], **Robert Gilkerson**[a,b]

[a]School of Integrative Biological & Chemical Sciences, The University of Texas Rio Grande Valley

[b]Medical Laboratory Sciences/Health & Biomedical Sciences, The University of Texas Rio Grande Valley

[c]Department of Biology, South Texas College

[d]Department of Pharmacology and Toxicology, University of Arkansas for Medical Sciences

Abstract

Mitochondrial optic atrophy-1 (OPA1) plays key roles in adapting mitochondrial structure to bioenergetic function. When transmembrane potential across the inner membrane ($\Delta\Psi_m$) is intact, long (L-OPA1) isoforms shape the inner membrane through membrane fusion and the formation of cristal junctions. When $\Delta\Psi_m$ is lost, however, OPA1 is cleaved to short, inactive S-OPA1 isoforms by the OMA1 metalloprotease, disrupting mitochondrial structure and priming cellular stress responses such as apoptosis. Previously, we demonstrated that L-OPA1 of H9c2 cardiomyoblasts is insensitive to loss of $\Delta\Psi_m$ via challenge with the protonophore carbonyl cyanide chlorophenyl hydrazone (CCCP), but that CCCP-induced OPA1 processing is activated upon differentiation in media with low serum supplemented with all-*trans* retinoic acid (ATRA). Here, we show that this developmental induction of OPA1 processing in H9c2 cells is independent of ATRA; moreover, pretreatment of undifferentiated H9c2s with chloramphenicol (CAP), an inhibitor of mitochondrial protein synthesis, recapitulates the $\Delta\Psi_m$-sensitive OPA1 processing observed in differentiated H9c2s. L6.C11 and C2C12 myoblast lines display the same developmental and CAP-sensitive induction of OPA1 processing, demonstrating a general mechanism of OPA1 regulation in mammalian myoblast cell settings. Restoration of CCCP-induced OPA1 processing correlates with increased apoptotic sensitivity. Moreover, *OPA1* knockdown indicates that intact OPA1 is necessary for effective myoblast differentiation. Taken together, our results indicate that

Correspondence: robert.gilkerson@utrgv.edu.
*These authors contributed equally

Conflict of interest

The authors declare that they have no conflicts of interest with the contents of this article.

a novel developmental mechanism acts to regulate OMA1-mediated OPA1 processing in myoblast cell lines, in which differentiation engages mitochondrial stress sensing.

Keywords

mitochondria; OPA1; OMA1; differentiation; transmembrane potential

1. Introduction

Mitochondria are increasingly found to participate in highly sensitive stress response mechanisms, allowing the organellar network to homeostatically maintain structure and function in response to cellular stimuli. Optic atrophy-1 (OPA1) plays a central role in regulating mitochondrial structure/function balance, mechanistically linking the transmembrane potential across the inner membrane ($\Delta\Psi_m$), generated by the complexes of oxidative phosphorylation (OXPHOS), with mitochondrial inner membrane fusion and cristae organization.

Located in the inner membrane, OPA1 plays crucial roles in shaping the inner membrane, mediating both fusion of the inner membrane and the formation of cristal junctions. To facilitate fusion of the inner membrane, OPA1 will either bind to itself (as a homodimer) or to mitochondrial-specific cardiolipin [1], allowing the mitochondria to organize as an interconnected network [2, 3]. At the same time, OPA1 also plays a key role in shaping mitochondrial cristae, the tubular/lamellar structuring of the inner membrane that provides an optimal environment for bioenergetics. The dimerization of the F_1F_0 ATP synthase establishes membrane curvature and tubulation of the cristae [4–7], while OPA1 associates with the mitochondrial cristae organizing system (MICOS) factors to organize the cristal junction, the ‘collar’ assembly where the tubular or lamellar cristae join the inner membrane [8]. Strikingly, the organization of the inner membrane into cristae provides for higher $\Delta\Psi_m$ values in the cristae relative to the inner membrane; moreover, this organization leads to heterogeneity of $\Delta\Psi_m$ in adjacent cristae [9]. OPA1’s role in cristal junction formation is mechanistically distinct from its role in mitochondrial fusion [10].

OPA1’s roles governing mitochondrial structure provide a unique link with bioenergetic function. Full-length, long OPA1 (L-OPA1) isoforms are located in the inner membrane, but are proteolytically cleaved upon loss of $\Delta\Psi_m$ to short S-OPA1 isoforms, which are released into the intermembrane space and are no longer functional at the inner membrane [2]. While the YME1L inner membrane protease carries out a constitutive, basal level of L-OPA1 processing at the S2 site, resulting in a steady-state balance of L-OPA1 and S-OPA1 isoforms, OMA1 is the stress-inducible metalloprotease that cleaves L-OPA1 isoforms: upon loss of $\Delta\Psi_m$, OMA1 cleaves OPA1 at the S1–site, causing accumulation of the S-OPA1 isoforms [11–13]; following proteolytic activation, OMA1 is then actively degraded [14]. The matrix-oriented N-terminal domain of OMA1 is required for $\Delta\Psi_m$ sensing [15], but the full mechanism by which OMA1 senses loss of $\Delta\Psi_m$ and activates OPA1 proteolysis remains unclear. Within the protein-dense inner membrane, OMA1 interacts with a range of factors, including AFG3L2 [16], cardiolipin [17], the prohibitins PHB1 and 2 [17, 18],

CHCHD2 and CHCHD10 [19], and YME1L [20, 21]. As a mitochondrial stress sensor, OMA1 has crucial impacts on cell-wide pathways including apoptosis and integrated stress response (ISR). Cleavage of L-OPA1 isoforms promotes apoptosis [2]: while L-OPA1 stabilizes mitochondrial cristae and prevents cytochrome c from exiting the organelle, cleavage of L-OPA1 disrupts cristal junctions, allowing these tightly-regulated collars to open and promote the efflux of cytochrome c to the cytosol, where it activates caspases for apoptosis [10]. OMA1 interacts directly with the pro-apoptotic factors Bax and Bak [22], as well as the MICOS complex [23], providing a direct mechanistic link between OMA1 and apoptotic induction. OMA1 also participates in integrated stress response (ISR), mediating mitochondria-to-nucleus retrograde signaling: mitochondrial stress causes OMA1 to cleave DELE1 to its short form, which is released to the cytosol, where it binds to and activates the heme regulated e1F-2 kinase (HRI), increasing translation of ATF4 and activating ISR [24, 25].

Previously, we demonstrated that H9c2 cardiomyoblasts fail to cleave L-OPA1 following challenge with the protonophore $\Delta\Psi_m$ uncoupler carbonyl cyanide m-chlorophenyl hydrazone (CCCP); however, differentiation using all-*trans* retinoic acid (ATRA) robustly induces CCCP-sensitive L-OPA1 processing, indicating that a developmental switch controls OMA1 in H9c2s [26]. These findings are consistent with an emerging literature suggesting key developmental roles for mitochondrial dynamics, with OPA1 playing a role in differentiation of stem cells to neurons [27, 28] and cardiac cells [29]. Specifically, myogenic differentiation involves a shift towards increased mitochondrial metabolism, with both increased mitochondrial biogenesis and quality control necessary for formation of differentiated muscle fibers [30], with OPA1 playing a critical role in metabolic reprogramming during muscle differentiation [31]. Here, we explore both the underlying mechanism and generality of this robust switch controlling stress-sensitive OPA1 processing.

2. Experimental procedures

2.1 Cell culture:

Cells were grown in high glucose Dulbecco's Modified Eagle's Medium (DMEM) with L-glutamine, phenol red, and sodium pyruvate (Gibco) supplemented with 10% fetal bovine serum (FBS) or 2% horse serum (HS) and antibiotic/antimycotic (Gibco) in a 5% CO_2 at 37 degrees C. H9c2, L6.C11, and C2C12 rat myoblasts were obtained from ATCC. For differentiation experiments, 350,000 cells were plated to 10 cm dishes in standard media. The next day, cells were given DMEM with 1% FBS with or without 1 μM ATRA and grown for five days. For CCCP treatment, cells were incubated with CCCP (from 10 mM stock in DMSO) at 10 μM for 1 hr. To monitor $\Delta\Psi_m$, tetramethyl rhodamine ester (TMRE) flow cytometry was used as previously [26, 32]: cells were incubated with 100 nM TMRE for 20 min., trypsinized, washed twice in PBS, and analyzed on a BD FACSCelesta. Flow cytometry data represent the mean fluorescence of 10,000 events in three independent biological replicates. To knock down OPA1 in C2C12s, the murine *OPA1* gene was disrupted by lentiviral transfection with shRNA constructs TRCN0000091111 (*OPA1* KD1) or TRCN0000091108 (*OPA1* KD2) (Millipore Sigma).

2.2 Immunoblotting:

For immunoblotting, cells were lysed in either RIPA, Laemmli, or 2X sample buffer (125 mM Tris-HCl 6.8, 2% SDS, 10% 2-mercapethanol, 20% glycerol, 0.05% bromophenol blue, 8 M urea). SDS-PAGE electrophoresis utilized 6% (for OPA1 blotting), 10% (for OMA1 blotting), or 4–20% (all others) gels. Antibodies used were: anti-OPA1 (1:1000, 612606 BD Biosci.), anti-OMA1 (1:1000, sc-515788 Santa Cruz), anti-MTCO1 ab14705 (1:1000, Abcam, Waltham, MA), anti-tubulin T6074 (1:1000, Sigma Aldrich), anti-cleaved caspase-3 (1:1000, Cell Signaling, Beverley, MA), goat anti-mouse poly-HRP (Invitrogen 32230), and goat anti-rabbit IgG (H+L) secondary antibody HRP (Invitrogen 31460). Jurkat cell apoptosis cell extracts without and with etoposide (Cell Signaling 2043S, Beverley, MA) were run as controls for STS experiments. Equal volumes of cell lysates were run on polyacrylamide gels (6% for OPA1, 10% for OMA1, 4–20% for all others) and transferred to Immobilon PVDF (Bio-Rad). Membranes were blocked in 5% milk in Tris-buffered saline + Tween (TBST), followed by primary and secondary antibody incubations. Blots were developed with West Dura SuperSignal (Thermo, 34076) and imaged using a GelDoc XR+ Gel Documentation System (Bio-Rad). Each blot shown is representative of at least three independent biological replicates. ImageJ quantification of Western blots also used at least three independent biological replicates.

2.3 Imaging:

For microscopic imaging, cells were seeded to glass coverslips. Coverslips were incubated in MitoTracker CMXRos (Invitrogen Molecular Probes, Eugene, OR) for 20 min. and washed with fresh media. Coverslips were fixed in 4% paraformaldehyde in PBS for 30 min. followed by permeabilization in 0.1% Triton X-100 in PBS for 10 min. Coverslips were then incubated in phalloidin-AlexaFluor488 (Invitrogen Molecular Probes, Eugene, OR) for 30 min., briefly counterstained with DAPI, and mounted with 50% glycerol in PBS. For cytochrome c immunolabeling experiments, cells were seeded to glass coverslips in 6-well dishes overnight, followed by transfection with mCherry-mito-7 (Addgene) using Lipofectamine 3000 (Invitrogen). Four hours post-transfection, cells were given fresh media and incubated for 48 hrs. Coverslips were fixed with 4% paraformaldehyde in PBS (30 min.), followed by antigen retrieval in 5% urea in 0.1 M Tris 8.8 at 95 degrees for 5 min. and permeabilization in 0.1% TX-100 in PBS. Coverslips were blocked in 10% normal goat serum (NGS) and incubated with anti-cytochrome c (Abcam ab110325) at 2 mg/mL in PBS for 1 hr, followed by washing 3 × 5 min. in PBS. Coverslips were then incubated in goat anti-mouse Alexa488 (Invitrogen Molecular Probes) at 1:100 dilution in PBS for 1 hr., washed 3 × 5 min. in PBS, counterstained with DAPI, and mounted in 50% glycerol in PBS. Samples were visualized on an Olympus Fluoview FV10i or Nikon AX confocal microscope at 60x.

2.4 Gene expression:

To examine gene expression, qRT-PCR was performed for *OPA1, OMA1, Bax, Bak*, and *MyoG*, as previously [26]. Cells were harvested from 10 cm cell culture dishes and total RNA processed using the QIAGEN RNeasy kit, followed by cDNA preparation using Superscript Reverse Transcriptase (Invitrogen).

Forward and reverse primers were used for the following *R. norvegicus* mRNAs: *OPA1*: F: CATACTAGGATCGGCTGTTGG R: ACTGTAACACACCCTTTAACT, *OMA1*: F: ATCCTCTAAGCCCTGCTTCC R: ATCCTCTAAGCCCTGCTTCC, *Bax:* F: TGCTAGCAAACTGGTGCTCA R: GGTCCCGAAGTAGGAAAGGA, *Bak:* F: AAGTTGCCCAGGACACAGAG R: TGTCCATCTCAGGGTTAGCA, *MyoG:* F: TCCAGTACATTGAGCGCCTA R: GCTGTGGGAGTTGCATTCAC, *ActB:* F: TGTCACCAACTGGGACGATA R: CTTTTCACGGTTGGCCTTAG. Murine *OPA1* primers were F: ACAGCATTTCGAGCAACAGA R: GCGCTCCAAGATCCTCTGAT. Samples were run on an Eco Illumina Real-time system (Illumina, San Diego, CA) using SyBr Green. Actin (*ActB*) was used to normalize expression levels.

2.5 OMA1 functional assay:

The OMA1 activity assay utilizes an 8-mer peptide (AFRATDHG) derived from the cleavage sequence of OPA1, which is reported to be specific of OMA1 which is referred as the OPA1 FRET substrate. The peptide contains a fluorogenic MCA moiety on the N-terminus and a DNP quencher moiety on the C-terminus, which was custom-synthesized by LifeTein LLC and handled accordingly to the manufacturer's instructions. Using a final 100 ul reaction volume and black, opaque 96 well plates (Costar), the reagents were added in the following order: 1) OMA1 activity assay buffer (50 mM of Tris/HCl, pH=7.5, 40 mM of KCl), 2) 5 μg of protein sample, and lastly, the OPA1 FRET substrate (5 μM final concentration; dissolved in DMSO). Fluorescence (RFU) was recorded (excitation/emission of 320/405 nm) once per minute for 30 min at 37°C using a fluorescent plate reader.

2.6 Statistical analyses:

Statistical analyses were carried out as previously [26, 33]. Data presented are the average mean of all samples ($n \geq 3$) ± standard error (SE). For OPA1 isoform and all other Western blotting quantifications, one-way analysis of variance (ANOVA) with Tukey's HSD was used. For comparison of mRNA expression, multinucleate cells, and cell density, results were analyzed via Student's *t*-test. In all experiments, $P < 0.05$ was considered statistically significant. * $P < 0.05$, ** $P < 0.01$, *** $P < 0.001$.

3. Results

3.1 Developmental induction of OPA1 processing is ATRA-independent.

Previously, we examined OPA1 processing in H9c2s differentiated in low serum media supplemented with ATRA (1% FBS+ATRA), following the method of Branco *et al.* [34]. While undifferentiated H9c2s do not undergo OPA1 processing in response to CCCP challenge, differentiation in low serum media with ATRA robustly restores CCCP-induced OPA1 cleavage [26]. To explore whether this induction of OPA1 processing is broadly activated by differentiation or is ATRA-specific, we passaged undifferentiated H9c2s in control media (10% FBS), or differentiated via growth in low serum media with ATRA (1% FBS +ATRA) or low serum alone (1% FBS). These two methods promote differentiation to either a more cardiac-like (low serum plus ATRA) or skeletal muscle-like (low serum alone) phenotype [35]. When grown in standard DMEM with 10% FBS, control H9c2 cells maintain a blast-type, rapidly-dividing morphology, as imaged by confocal microscopy.

Upon differentiation with ATRA (1% FBS+ATRA), however, H9c2s adopt a more elongate, cardiomyocyte-like morphology. H9c2s grown in low serum media *lacking* ATRA (1% FBS) show a tube-like, spindled morphology consistent with a skeletal muscle-like phenotype (Fig. 1A). To examine relative differences in gene expression in these three different growth conditions, quantitative reverse transcriptase PCR (qRT-PCR) was performed to examine the abundance of several mRNAs. Relative to control H9c2s, 1% FBS+ATRA cells displayed increased relative expression of *OPA1, OMA1, Bax, Bak*, and the muscle marker *MyoG*. Strikingly, H9c2s differentiated *without* ATRA (1% FBS) displayed significant *decreases* in these same factors (Fig. 1B). Thus, differentiation of H9c2s with or without ATRA provokes marked differences in genetic and phenotypic readouts, consistent with, and expanding on, the results of Branco *et al.* [34].

We next explored $\Delta\Psi_m$-sensitive OPA1 processing by challenging these cells with 10 μM CCCP for 1 hr. In the absence of CCCP challenge, all three media conditions (control, 1% FBS+ATRA, 1% FBS) maintained both L-OPA1 isoforms (upper two bands) and S-OPA1 isoforms (lower three bands). Under CCCP challenge, control (undifferentiated) H9c2s retained L-OPA1 isoforms, as we had shown previously [26]. Strikingly, CCCP challenge of H9c2s differentiated with either 1% FBS+ATRA or 1% FBS alone resulted in robust cleavage of L-OPA1 isoforms (Fig. 1C). ImageJ quantification of OPA1 isoforms confirms this: control H9c2s retain L-OPA1 both without (60±1%) and with (50±3%) CCCP challenge, while H9c2s differentiated with 1% FBS+ATRA show a significant decrease in L-OPA1, from 58±2% (without CCCP) to 12±2% (with CCCP). Similarly, H9c2s differentiated with 1% FBS alone drop from 59±2% (without CCCP) to 12±3% (with CCCP). Further, both differentiated conditions show a significant difference under CCCP challenge compared with control H9c2s+CCCP ($p<0.01$) (Fig. 1D). These results demonstrate that while differentiation of H9c2s in 1% FBS+ATRA or 1% FBS alone provokes very distinct cellular gene expression and morphology phenotypes, *both* conditions robustly activate CCCP-induced OPA1 processing.

As OMA1 is the major identified $\Delta\Psi_m$-sensitive OPA1 protease, we next examined OMA1 status in control versus differentiated H9c2s. Following loss of $\Delta\Psi_m$, OMA1 undergoes activation followed by degradation: one hour of CCCP challenge is sufficient to induce L-OPA1 cleavage, followed by loss of OMA1 several hours later [14, 20]. We therefore examined control and differentiated H9c2s without and with 4 hr. CCCP challenge. Undifferentiated control H9c2s retain a strong OMA1 band both without and with 4 hrs. of CCCP challenge, as previously. While differentiated H9c2s (both 1% FBS+ATRA and 1% FBS) show a strong band for OMA1, both show a marked decrease in OMA1 following CCCP challenge (Fig. 1E). This is confirmed by quantitation of OMA1 immunoblots, which demonstrate significant decreases in differentiated H9c2s following 4 hrs. of CCCP treatment, but not in controls (Fig. 1F). These results are consistent with a lack of OMA1 activation and degradation in undifferentiated H9c2s, as well as a robust induction of OMA1 activation and degradation upon CCCP challenge in both 1% FBS+ATRA and 1% FBS H9c2 differentiation settings. As a parallel independent approach, OMA1 activity was examined using a cell-free assay. This OMA1 functional assay tests the ability of OMA1 in cellular lysates to cleave an OPA1 peptide reporter, which then produces a fluorescence signal [36]. Cell lysates were incubated with the OPA1 peptide reporter and fluorescence

was monitored for 30 min (excitation 325 nm/emission 392 nm) (Fig. 1G). Importantly, OMA1 functional activity was statistically equivalent in untreated H9c2s compared to both differentiation treatments (Fig. 1H). This indicates that OMA1 is fully capable of cleaving OPA1 in undifferentiated H9c2s, but that within the mitochondrial inner membrane *in situ*, OMA1 is inhibited by an unknown interacting partner or partners.

Taken together, these results show that two very distinct differentiation programs activate $\Delta\Psi_m$-sensitive OPA1 processing in H9c2s, indicating that CCCP challenge causes OMA1's activation and cleavage of L-OPA1 isoforms, followed by degradation of OMA1. This developmental switch is therefore not dependent on ATRA alone but is more broadly activated by cellular differentiation.

3.2 Disruption of mitochondrial protein synthesis engages OPA1 processing in undifferentiated H9c2s.

To explore the mechanism of this intriguing switch, we examined whether the developmental induction of CCCP-sensitive OPA1 processing could be recapitulated in undifferentiated H9c2s. In mammalian cells, chloramphenicol (CAP) binds to the mitochondrial (but not cytosolic) ribosome and prevents peptides from exiting, thus shutting down synthesis of mtDNA-encoded proteins [37]. Disruption of mitochondrial protein synthesis triggers cell-wide stress response [38]. We hypothesized that CAP-mediated inhibition of mitochondrial protein synthesis might engage $\Delta\Psi_m$-sensitive OPA1 processing in undifferentiated H9c2s subsequently challenged with CCCP. To test this, undifferentiated H9c2s were incubated with 40 μg/ml CAP for 72 hrs. followed by addition of CCCP for 1 hr. Control H9c2s displayed L-OPA1 isoforms both without and with CCCP challenge, as above (Fig. 1C), as did H9c2s incubated with CAP alone. H9c2s treated with CAP, followed by CCCP challenge, however, displayed a total loss of L-OPA1 isoforms (Fig. 2A). This loss of L-OPA1 was confirmed by ImageJ quantification: while untreated (52±6%) versus CCCP-treated (41±7%) did not show a significant loss of L-OPA1, CAP-treated H9c2s (66±1%) showed a sharp decrease under CCCP challenge (10±4%) (Fig. 2B). Further, *OMA1*−/− cells displayed strong L-OPA1, even in the presence of CCCP (Fig. 2A). These results demonstrate that CAP treatment robustly activates CCCP-induced OPA1 processing in undifferentiated H9c2s, consistent with CAP-mediated activation of OMA1. Immunoblotting for the mtDNA-encoded MTCO1 protein demonstrated that while untreated control and CCCP-challenged H9c2s show a strong band for MTCO1, CAP-treated H9c2s show no signal for MTCO1 (Fig. 2C), consistent with complete inhibition of mitochondrial protein synthesis by CAP, as expected. OMA1 immunoblotting revealed that control H9c2s challenged with CCCP (1 or 4 hrs.) retain OMA1 signal. CAP-treated H9c2s challenged with CCCP for 4 hrs, however, showed a decrease in OMA1 signal (Fig. 2D), consistent with activation and subsequent degradation of OMA1, as above (Fig. 1E). OMA1 immunoblot quantitation confirms significant loss of OMA1 in CAP-treated cells under CCCP challenge, but not in controls (Fig. 2E). These findings demonstrate that inhibition of mitochondrial protein synthesis via CAP engages $\Delta\Psi_m$-sensitive OPA1 processing in undifferentiated H9c2s, recapitulating the activation observed in differentiated H9c2s above (Fig. 1). Flow cytometric analysis of relative $\Delta\Psi_m$ using the Nernstian dye tetramethyl rhodamine ester (TMRE) show that CCCP challenge elicits equivalent loss of $\Delta\Psi_m$ in

untreated control and CAP-treated H9c2s (Fig. 2F). Since disruption of mitochondrial protein synthesis in undifferentiated H9c2s recapitulates the activation of OPA1 processing found in differentiated H9c2s (Fig. 1), we tested whether the activation of OPA1 processing in differentiated H9c2s is accompanied by a decrease in mitochondrial protein synthesis. We examined the relative levels of mtDNA-encoded MTCO1 in undifferentiated control H9c2s as compared with differentiated H9c2s. While control H9c2s show a strong signal for MTCO1, CAP-treated H9c2s show no signal, as above. H9c2s differentiated with either 1% FBS+ATRA or 1% FBS alone show levels of MTCO1 equivalent to that of control H9c2s (Fig. 2G); immunoblot quantification confirms significant loss of MTCO1 in CAP-treated H9c2s, but not in differentiated H9c2s (Fig. 2H). These results indicate that mtDNA-derived proteins are not decreased in differentiated H9c2s, suggesting that the observed activation of CCCP-induced OPA1 processing is not driven by loss of mtDNA-encoded protein synthesis *per se*.

To further explore the impact of mitochondrial protein synthesis on OPA1 processing, we examined the effect of actinonin (ACT). While CAP shuts down ribosomal protein synthesis altogether, ACT induces stalling of the mitoribosome, causing proteostatic stress within the mitochondrial inner membrane through the accumulation of faulty mtDNA-encoded polypeptides [39]. While untreated control H9c2s retained both L- and S-OPA1 isoforms, ACT-treated H9c2s showed an accumulation of S-OPA1, though they retained some L-OPA1. Co-treatment with ACT and CAP blunted this processing, with full L-OPA1 retained (Fig. 2I). ImageJ quantification confirmed that ACT induced a significant loss of L-OPA1 (30±4%) versus untreated controls (59±5%), while ACT+CAP (57±2%) was equivalent to untreated controls (Fig. 2J). Taken together, these results indicate that CAP-mediated inhibition of the mitochondrial ribosome acts to engage CCCP-induced OPA1 processing in undifferentiated H9c2s, while ACT-induced proteostatic stress is sufficient to partially activate OPA1 processing even in the absence of CCCP. These results suggest that uncharacterized heterotypic protein-protein interactions at the inner membrane are responsible for the induction of OPA1 processing observed in H9c2s. The prohibitins PHB1 and PHB2 are inner membrane scaffolding proteins that interact with cardiolipin [18] and OMA1 [17] to modulate OMA1 in a large complex, while PHB2 deletion causes loss of L-OPA1 isoforms [40], suggesting that the observed activation of OPA1 processing might be mediated by modulation of PHB levels. However, no difference in PHB2 was observed in comparing control H9c2s versus CAP-treated or differentiated H9c2s (Fig. 2K), with no significant differences in PHB2 levels found by quantification (Fig. 2I).

3.3 L6.C11 and C2C12 myoblasts activate OPA1 processing.

To explore whether the developmental activation of OPA1 processing observed in H9c2 cells occurs in other cell settings, we examined rat L6.C11 and murine C2C12 myoblasts. OPA1 Western blots of L6.C11 cells grown in standard media show the expected balance of L-OPA1 and S-OPA1 isoforms. Strikingly, L6.C11s retain L-OPA1 isoforms under CCCP challenge (two biological replicates shown, Fig. 3A), with equivalent L-OPA1 levels without (65±1%) or with CCCP (51±8%) (Fig. 3B). Similarly, C2C12 myoblasts retain strong L-OPA1 under CCCP challenge (Fig. 3C), with only a modest loss of L-OPA1 in CCCP-treated (50±1%) versus untreated C2C12s (60±2%) (Fig. 3D). These results demonstrate that

CCCP fails to induce the full cleavage of L-OPA1 in both L6.C11 and C2C12 myoblast lines, recapitulating the CCCP insensitivity observed in undifferentiated H9c2s (Fig. 1C). To explore whether differentiation might activate CCCP-induced OPA1 processing as in H9c2s, L6.C11 myoblasts were differentiated using media with either 1% FBS or 1% FBS +ATRA, as in H9c2s (Fig. 1). Confocal imaging shows that control L6.C11s have the expected blast-type morphology of rapidly-diving cells, while L6.C11s differentiated in 1% FBS, either with or without ATRA, adopt a more elongate, spindled morphology (Fig. 3E), consistent with muscle-like differentiation. C2C12s display a similar shift in cellular morphology, transitioning from a small, rapidly-dividing blast morphology to a larger, more spindled state (Fig. 3F). Analysis of gene expression in control versus 1%FBS+ATRA and 1%FBS differentiated C2C12s reveals that both differentiation regimes elicit strong increases in myogenic differentiation factors *MyoG*, *MyoM2*, and *DMD*. In addition, the mitophagic factor *Parkin* is robustly induced by both differentiation methods (Fig. 3G), consistent with a key role for mitophagy in myogenic differentiation [41]. These data demonstrate that both L6C11 and C2C12 myoblast lines undergo similar differentiation to H9c2s.

To test whether L6.C11 and C2C12 myoblasts employ a developmental switch to activate $\Delta\Psi_m$-sensitive OPA1 processing as in H9c2s, we examined OPA1 in differentiated L6.C11s and C2C12s, as well as in undifferentiated myoblasts grown in the presence of CAP. While undifferentiated control L6.C11s retained L-OPA1 in both the absence or presence of CCCP, L6.C11s grown in CAP show robust cleavage of L-OPA1 when challenged with CCCP. Similarly, L6.C11s differentiated with either 1% FBS+ATRA or 1% FBS alone display full, robust L-OPA1 cleavage under CCCP challenge (Fig. 4A). ImageJ quantification of L-OPA1 isoforms confirms that CCCP challenge elicits a significantly greater loss of L-OPA1 in CAP-treated (20±5%) or differentiated (1% FBS+ATRA (14±1%) or 1% FBS (16±3%)) as compared with CCCP-treated control L6C11s (34±2%) (Fig. 4B). Similarly, control C2C12s maintain L-OPA1 isoforms both without and with CCCP challenge, but show robust L-OPA1 cleavage under CCCP challenge in CAP-treated and differentiated (1% FBS+ATRA and 1% FBS) C2C12s (Fig. 4C). Quantification of L-OPA1 confirms that CCCP induces significantly greater cleavage of L-OPA1 in CAP-treated (18±2%) or differentiated (1% FBS+ATRA (23±4%) or 1% FBS (15±1%)) as compared with CCCP-treated control C2C12s (44±5%) (Fig. 4D). These findings demonstrate that both L6.C11 and C2C12 myoblasts show developmental activation of OPA1 processing in response to both differentiation and CAP treatment, recapitulating the induction shown for H9c2s (Fig. 1). To examine whether the induction of OPA1 processing is consistent with OMA1 activation in these cell lines, we examined whether OMA1 was degraded in response to 4 hr. CCCP challenge, as above (Fig. 1E). Control L6.C11s show a strong band for OMA1 both without and with CCCP challenge, while OMA1−/− knockout MEFs show no band, demonstrating the specificity of the antibody. CAP-treated and differentiated (1% FBS+ATRA and 1% FBS) L6.C11 lysates show a strong band for OMA1; however, this band is absent or greatly reduced under CCCP challenge (Fig. 4E). OMA1 immunoblot quantification confirms that differentiated L6.C11s show significant loss of OMA1 upon 4 hr. CCCP challenge, as compared with CCCP-challenged controls (Fig. 4F). Similarly, control C2C12s show a strong band for OMA1 both without and with CCCP challenge, while CAP-treated and differentiated C2C12s show a strong OMA1 band that is lost upon

CCCP challenge (Fig. 4G). ImageJ quantification confirms a significant loss of OMA1 signal in CAP-treated and differentiated C2C12s as compared with CCCP-treated controls (Fig. 4H). These results demonstrate that rat L6.C11 and murine C2C12 myoblast lines share the insensitivity to CCCP observed in H9c2s, and also recapitulate the activation of OPA1 processing induced by either inhibition of mitochondrial protein synthesis or differentiation observed in H9c2s. Taken together, these results strongly indicate that OMA1-mediated $\Delta\Psi_m$-sensitive OPA1 processing can be turned on or off as a general mechanism of myoblast cell settings.

3.4 Induction of OPA1 processing correlates with increased apoptotic sensitivity and disruption of differentiation.

OPA1 plays a strong anti-apoptotic role through its regulation of cristal structure within the inner membrane: under basal conditions, OPA1 maintains cristal junctions and restricts the release of cytochrome c, while apoptotic induction disrupts cristae maintenance and allows efflux of cytochrome c into the cytosol, activating apoptotic caspases [10]. Thus, L-OPA1 isoforms protect the cell against apoptosis [11, 42]. We therefore hypothesized that activation of OPA1 processing in H9c2s will confer increased apoptotic sensitivity in myoblast cells. To test this hypothesis, untreated control and CAP-treated H9c2s were challenged with staurosporine (STS), a canonical inducer of mitochondrial apoptosis: STS treatment elicits the release of mitochondrial cytochrome c into the cytosol, followed by caspase activation and subsequent cell death [43, 44]. When incubated with CCCP in either the absence or presence of CAP, H9c2s show typical blast-type cell morphology, as visualized by phalloidin labeling of the actin cytoskeleton and DAPI staining of nuclei. Upon STS challenge for 2 hrs in the presence of CCCP, H9c2s without CAP show a disorganized actin cytoskeleton, consistent with STS-induced disruption of actin microfilaments [45]. H9c2s challenged with STS in the presence of CAP, however, transition to a shrunken cell morphology with withered projections (Fig. 5A), consistent with robust induction of apoptosis. In parallel, confocal immunofluorescence microscopy was used to examine cytochrome c release: control H9c2 cells show colocalization of cytochrome c immunolabeling (green) with mCherry-mito, a transfectable marker of mitochondrial localization (red), in the absence or presence of STS treatment, as do CAP-treated H9c2s in the absence of STS. STS-treated H9c2s show mitochondrial localization of cytochrome c, with some apparent cytosolic signal (see Fig. 5B, detail). When CAP-treated H9c2s are challenged with STS, however, cytochrome c signal can be found in the cytoplasm, rather than sequestered within the mitochondrial network (Fig. 5B), indicating that STS challenge in CAP-treated H9c2s induces cytochrome c release. As an additional means of assaying apoptotic induction, we performed Western blotting for cleaved caspase-3 on H9c2s under these conditions. In the presence of CCCP alone, control H9c2s show little signal for cleaved caspase-3, consistent with minimal apoptotic induction. When challenged with 1 μM STS for 2 hrs, a modest increase in cleaved casp-3 is observed, consistent with a small boost in apoptosis. CAP-treated H9c2s given CCCP alone similarly show little or no signal for cleaved caspase-3. When challenged with STS in the presence of CCCP, however, CAP-treated H9c2s show a strong cleaved caspase-3 signal, consistent with a strong induction of apoptosis. As a control for cleaved caspase-3 as a marker of apoptotic induction, manufacturer-provided lysates from Jurkat cells without and with the apoptotic inducer

etoposide (Cell Signaling) show a strong cleaved caspase-3 signal in etoposide-treated cells indicative of robust apoptosis (Fig. 5C). ImageJ quantification confirms that CAP-treated H9c2s show a significantly stronger induction of cleaved caspase-3 in response to STS treatment compared with STS-treated controls (1.55±0.2 versus 0.56±0.3, respectively) (Fig. 5D). These results indicate that CAP sensitizes H9c2s to STS-induced apoptosis. To test whether CCCP-mediated OPA1 processing confers increased apoptotic sensitivity, CAP-treated H9c2s were challenged with STS in the absence or presence of CCCP. CAP-treated H9c2s in the absence of STS display blast-type cell morphology with a well-developed actin cytoskeleton. H9c2s challenged with STS in the absence of CCCP display a disorganized actin distribution, as in 5A. H9c2s challenged with STS in the presence of CCCP, however, show a shrunken morphology with fragmented cell processes (Fig. 5E). Western blotting for cleaved caspase-3 shows a modest increase in signal for H9c2s challenged with STS in the absence of CCCP, while a stronger signal is observed in CCCP-treated H9c2s challenged with STS (Fig. 5F). ImageJ quantification confirms significant increases in cleaved caspase-3 in STS-challenged H9c2s, with CCCP-treated STS-challenged H9c2s showing a significantly greater signal than STS-challenged H9c2s lacking CCCP (Fig. 5G). Taken together, these results are consistent with heightened apoptotic sensitivity in cells with fully engaged $\Delta\Psi_m$-sensitive OPA1 processing.

Recent findings suggest that OPA1 may have important developmental roles: disruption of OPA1 interferes with cardiomyocyte [29] and neural differentiation [27]. To explore whether OPA1 is needed for effective myoblast differentiation, H9c2s were differentiated (in media containing 1% FBS+ATRA or 1% FBS alone, as above) for 24 hrs. in the presence or absence of CCCP, alongside undifferentiated controls. Undifferentiated control H9c2s maintain a blast-type morphology both without and with 24 hrs. of CCCP treatment. After 24 hrs. in differentiation media, H9c2s (in either 1% FBS+ATRA or 1% FBS alone) without CCCP show a largely blast-type morphology. Strikingly, however, H9c2s differentiated while under CCCP challenge display a smaller, shrunken morphology (Fig. 6A). Further, while undifferentiated control H9c2s have equivalent cell density without or with CCCP, differentiated H9c2s (both 1% FBS+ATRA or 1% FBS alone) treated with CCCP show significant decreases in cell density compared with differentiated H9c2s lacking CCCP (Fig. 6B). As an alternate approach, differentiation of myoblasts in media with 2% horse serum (HS) elicits a strong myogenic phenotype, in which myoblasts develop into long, multinucleate fibers [41, 46]. Control C2C12s differentiated for 6 d. in 2% HS display long, multinucleate fibers by confocal microscopy. *OPA1* knockdown (KD1 and KD2) myoblasts, however, fail to establish muscle-like fibers (Fig. 6E), with significantly fewer multinucleate cells than controls (Fig. 6F) and decreased cell density (Fig. 6G). Analysis of relative gene expression reveals that OPA1 knockdown causes significant decreases in expression of key myogenic genes *MyoG*, *MyoM2*, and *Mef2c* (Fig. 6H). These results, using pharmacologic and genetic approaches to reduce L-OPA1, demonstrate that loss of OPA1 disrupts myoblast differentiation, consistent with a key role for OPA1 in muscle development. Taken together, our results suggest that the developmental switch controlling OPA1 processing in myoblasts has important implications for both apoptotic sensitivity and differentiation.

4. Discussion

Our results present two novel aspects of stress-sensitive mitochondrial OPA1 processing. First, a potent molecular switch, or 'clutch', is capable of activating $\Delta\Psi_m$-sensitive OPA1 processing, in which cleavage of L-OPA1 isoforms following CCCP challenge is restored. This 'clutch' can be engaged either by cellular differentiation or inhibition of mitochondrial protein synthesis. Second, this switch is a general phenomenon of myoblast cell lines, indicating that activation of stress-sensitive OPA1 processing is part of muscle-type differentiation programs, contributing to cellular stress sensing in post-mitotic cells.

While it remains unclear precisely how decreases in $\Delta\Psi_m$ initiate OMA1's proteolytic cleavage of L-OPA1, some key mechanistic determinants of OMA1's stress-sensitive activation have been identified. For example, the positively-charged residues in the matrix-exposed N-terminal domain of OMA1 appear to be required for $\Delta\Psi_m$ sensing and activation of the IMS-facing M48 metallopeptidase domain [15], while studies in yeast indicate that disulfide bonding between cysteine residues located on the IMS side of the membrane are critical for OMA1 redox sensing and stability [47]. Our results suggest an additional level of regulation, demonstrating that stress-sensitive OPA1 cleavage can be turned on or off by an uncharacterized mechanism. This underlying mechanism likely involves one or more of OMA1's interacting partners, and potentially involves higher-order organization within the inner membrane. As OMA1 interacts directly with membrane-shaping factors such as the MICOS-integral Mic60 [23], cardiolipin, and prohibitins [17, 18], a higher-order macromolecular domain including OMA1 and associated factors may serve to mediate OMA1's various stress-responsive roles within the protein-dense mitochondrial inner membrane. This may include interaction with OXPHOS complexes: our results indicate that inhibition of the mitoribosome (via CAP treatment) engages CCCP-induced OPA1 processing, but that this engagement is not mediated by a broad loss of mtDNA-encoded polypeptides, as differentiated H9c2s still maintain steady-state levels of MTCO1. Work in progress is exploring the involvement of both known OMA1-interacting factors and mtDNA-encoded factors in mediating the observed 'switch' for activation of OPA1 processing. Moreover, understanding the arrangement of OMA1 with its interacting factors within the inner membrane is an important next goal. The arrangement of associated mitochondrial factors in higher-order localized domains within the IM is an emerging mechanism of Coenzyme Q maintenance [48], mitochondrial translation and complex assembly [49], and TOM/TIM protein import [50], providing for both mitochondrial functionalities and crosstalk with ER contact sites [48, 51].

While the importance of stress-sensitive OMA1 activation and subsequent OPA1 processing to cell-wide pathways such as apoptosis [10, 52] and integrated stress response [24, 25] is increasingly appreciated, our results also suggest a novel role for stress-sensitive OPA1 processing as part of developmental reprogramming during differentiation. An emerging literature indicates that mitochondrial dynamics are integrally involved in cellular differentiation in a variety of cell settings: OPA1 (together with MFN1) is required for effective maintenance of germline stem cells in *Drosophila melanogaster* [53], while OPA1 is also needed for neural cell specification [27]. Intriguingly, interrupting OPA1-mediated mitochondrial fusion in mouse embryonic stem cells interferes with cardiomyocyte

differentiation not through bioenergetic deficiency, but via increased calcineurin-Notch1 signaling [29]. Our results add to this emerging role for mitochondrial OPA1, indicating that activation of stress-sensitive mitochondrial processing contributes to differentiation of myoblast cells. During myogenic differentiation, myoblasts undergo mitochondrial remodeling, consisting of rapid mitophagy, followed by mitochondrial biogenesis [41, 46]. Our results indicate that OPA1 is necessary for effective myogenic differentiation (Fig. 6), consistent with findings that OPA1 plays a key role in myoblast metabolic switching [31]. While the role of mitochondrial OPA1 processing in differentiation is likely to be highly context-dependent, future work will examine the impacts of OPA1 processing on myocyte differentiation, as well as other developmental contexts that echo the activation observed here.

Acknowledgements

This work was supported by NIGMS 2SC3GM116669 (to R.G.) and 1SC3GM132053 (to M.K.). The content is solely the responsibility of the authors and does not necessarily represent the official views of the National Institutes of Health. H.K. and P.D.L.T. were supported by the UTRGV Presidential Graduate Research Award. We thank Dr. Tobias Weinrich for helpful discussions.

Abbreviations

ATRA	all-*trans* retinoic acid
CAP	chloramphenicol
CCCP	carbonyl cyanide *m*-chlorophenyl hydrazone
DAPI	diaminophenylindole
DMEM	Dulbecco's Modified Eagle's Medium
FBS	fetal bovine serum
HS	horse serum
MEFs	mouse embryonic fibroblasts
NGS	normal goat serum
OXPHOS	oxidative phosphorylation
PBS	phosphate-buffered saline
SE	standard error
STS	staurosporine
TBST	Tris-buffered saline plus Tween
$\Delta\Psi_m$	transmembrane potential across the mitochondrial inner membrane

References

1. Ban T, Ishihara T, Kohno H, Saita S, Ichimura A, Maenaka K, et al. , Molecular basis of selective mitochondrial fusion by heterotypic action between OPA1 and cardiolipin. Nat Cell Biol, 2017. 19(7): p. 856–863. [PubMed: 28628083]
2. Griparic L, Kanazawa T, and van der Bliek AM, Regulation of the mitochondrial dynamin-like protein Opa1 by proteolytic cleavage. J Cell Biol, 2007. 178(5): p. 757–64. [PubMed: 17709430]
3. Ishihara N, Fujita Y, Oka T, and Mihara K, Regulation of mitochondrial morphology through proteolytic cleavage of OPA1. EMBO J, 2006. 25(13): p. 2966–77. [PubMed: 16778770]
4. Paumard P, Vaillier J, Coulary B, Schaeffer J, Soubannier V, Mueller DM, et al. , The ATP synthase is involved in generating mitochondrial cristae morphology. EMBO J, 2002. 21(3): p. 221–30. [PubMed: 11823415]
5. Minauro-Sanmiguel F, Wilkens S, and Garcia JJ, Structure of dimeric mitochondrial ATP synthase: novel F0 bridging features and the structural basis of mitochondrial cristae biogenesis. Proc Natl Acad Sci U S A, 2005. 102(35): p. 12356–8. [PubMed: 16105947]
6. Strauss M, Hofhaus G, Schroder RR, and Kuhlbrandt W, Dimer ribbons of ATP synthase shape the inner mitochondrial membrane. EMBO J, 2008. 27(7): p. 1154–60. [PubMed: 18323778]
7. Hahn A, Parey K, Bublitz M, Mills DJ, Zickermann V, Vonck J, et al. , Structure of a Complete ATP Synthase Dimer Reveals the Molecular Basis of Inner Mitochondrial Membrane Morphology. Mol Cell, 2016. 63(3): p. 445–56. [PubMed: 27373333]
8. Stephan T, Bruser C, Deckers M, Steyer AM, Balzarotti F, Barbot M, et al. , MICOS assembly controls mitochondrial inner membrane remodeling and crista junction redistribution to mediate cristae formation. EMBO J, 2020. 39(14): p. e104105. [PubMed: 32567732]
9. Wolf DM, Segawa M, Kondadi AK, Anand R, Bailey ST, Reichert AS, et al. , Individual cristae within the same mitochondrion display different membrane potentials and are functionally independent. EMBO J, 2019. 38(22): p. e101056. [PubMed: 31609012]
10. Frezza C, Cipolat S, Martins de Brito O, Micaroni M, Beznoussenko GV, Rudka T, et al. , OPA1 controls apoptotic cristae remodeling independently from mitochondrial fusion. Cell, 2006. 126(1): p. 177–89. [PubMed: 16839885]
11. Anand R, Wai T, Baker MJ, Kladt N, Schauss AC, Rugarli E, et al. , The i-AAA protease YME1L and OMA1 cleave OPA1 to balance mitochondrial fusion and fission. J Cell Biol, 2014. 204(6): p. 919–29. [PubMed: 24616225]
12. Ehses S, Raschke I, Mancuso G, Bernacchia A, Geimer S, Tondera D, et al. , Regulation of OPA1 processing and mitochondrial fusion by m-AAA protease isoenzymes and OMA1. J Cell Biol, 2009. 187(7): p. 1023–36. [PubMed: 20038678]
13. Head B, Griparic L, Amiri M, Gandre-Babbe S, and van der Bliek AM, Inducible proteolytic inactivation of OPA1 mediated by the OMA1 protease in mammalian cells. J Cell Biol, 2009. 187(7): p. 959–66. [PubMed: 20038677]
14. Zhang K, Li H, and Song Z, Membrane depolarization activates the mitochondrial protease OMA1 by stimulating self-cleavage. EMBO Rep, 2014. 15(5): p. 576–85. [PubMed: 24719224]
15. Baker MJ, Lampe PA, Stojanovski D, Korwitz A, Anand R, Tatsuta T, et al. , Stress-induced OMA1 activation and autocatalytic turnover regulate OPA1-dependent mitochondrial dynamics. EMBO J, 2014. 33(6): p. 578–93. [PubMed: 24550258]
16. Consolato F, Maltecca F, Tulli S, Sambri I, and Casari G, m-AAA and i-AAA complexes coordinate to regulate OMA1, the stress-activated supervisor of mitochondrial dynamics. J Cell Sci, 2018. 131(7).
17. Anderson CJ, Kahl A, Fruitman H, Qian L, Zhou P, Manfredi G, et al. , Prohibitin levels regulate OMA1 activity and turnover in neurons. Cell Death Differ, 2019.
18. Richter-Dennerlein R, Korwitz A, Haag M, Tatsuta T, Dargazanli S, Baker M, et al. , DNAJC19, a mitochondrial cochaperone associated with cardiomyopathy, forms a complex with prohibitins to regulate cardiolipin remodeling. Cell Metab, 2014. 20(1): p. 158–71. [PubMed: 24856930]
19. Ruan Y, Hu J, Che Y, Liu Y, Luo Z, Cheng J, et al. , CHCHD2 and CHCHD10 regulate mitochondrial dynamics and integrated stress response. Cell Death Dis, 2022. 13(2): p. 156. [PubMed: 35173147]

20. Rainbolt TK, Lebeau J, Puchades C, and Wiseman RL, Reciprocal Degradation of YME1L and OMA1 Adapts Mitochondrial Proteolytic Activity during Stress. Cell Rep, 2016. 14(9): p. 2041–2049. [PubMed: 26923599]
21. MacVicar TD and Lane JD, Impaired OMA1-dependent cleavage of OPA1 and reduced DRP1 fission activity combine to prevent mitophagy in cells that are dependent on oxidative phosphorylation. J Cell Sci, 2014. 127(Pt 10): p. 2313–25. [PubMed: 24634514]
22. Jiang X, Jiang H, Shen Z, and Wang X, Activation of mitochondrial protease OMA1 by Bax and Bak promotes cytochrome c release during apoptosis. Proc Natl Acad Sci U S A, 2014. 111(41): p. 14782–7. [PubMed: 25275009]
23. Viana MP, Levytskyy RM, Anand R, Reichert AS, and Khalimonchuk O, Protease OMA1 modulates mitochondrial bioenergetics and ultrastructure through dynamic association with MICOS complex. iScience, 2021. 24(2): p. 102119. [PubMed: 33644718]
24. Guo X, Aviles G, Liu Y, Tian R, Unger BA, Lin YT, et al. , Mitochondrial stress is relayed to the cytosol by an OMA1-DELE1-HRI pathway. Nature, 2020. 579(7799): p. 427–432. [PubMed: 32132707]
25. Fessler E, Eckl EM, Schmitt S, Mancilla IA, Meyer-Bender MF, Hanf M, et al. , A pathway coordinated by DELE1 relays mitochondrial stress to the cytosol. Nature, 2020. 579(7799): p. 433–437. [PubMed: 32132706]
26. Garcia I, Calderon F, la Torre P, Vallier SS, Rodriguez C, Agarwala D, et al. , Mitochondrial OPA1 cleavage is reversibly activated by differentiation of H9c2 cardiomyoblasts. Mitochondrion, 2021. 57: p. 88–96. [PubMed: 33383158]
27. Caglayan S, Hashim A, Cieslar-Pobuda A, Jensen V, Behringer S, Talug B, et al. , Optic Atrophy 1 Controls Human Neuronal Development by Preventing Aberrant Nuclear DNA Methylation. iScience, 2020. 23(6): p. 101154. [PubMed: 32450518]
28. Jonikas M, Madill M, Mathy A, Zekoll T, Zois CE, Wigfield S, et al. , Stem cell modeling of mitochondrial parkinsonism reveals key functions of OPA1. Ann Neurol, 2018. 83(5): p. 915–925. [PubMed: 29604226]
29. Kasahara A, Cipolat S, Chen Y, Dorn GW 2nd, and Scorrano L, Mitochondrial fusion directs cardiomyocyte differentiation via calcineurin and Notch signaling. Science, 2013. 342(6159): p. 734–7. [PubMed: 24091702]
30. Hong X, Isern J, Campanario S, Perdiguero E, Ramirez-Pardo I, Segales J, et al. , Mitochondrial dynamics maintain muscle stem cell regenerative competence throughout adult life by regulating metabolism and mitophagy. Cell Stem Cell, 2022. 29(10): p. 1506–1508. [PubMed: 36206734]
31. Triolo M, Baker N, Agarwal S, Larionov N, Podinic T, and Khacho M, Optic atrophy 1 mediates muscle differentiation by promoting a metabolic switch via the supercomplex assembly factor SCAF1. iScience, 2024. 27(3): p. 109164. [PubMed: 38414856]
32. Jones E, Gaytan N, Garcia I, Herrera A, Ramos M, Agarwala D, et al. , A threshold of transmembrane potential is required for mitochondrial dynamic balance mediated by DRP1 and OMA1. Cell Mol Life Sci, 2017. 74(7): p. 1347–1363. [PubMed: 27858084]
33. Garcia I, Innis-Whitehouse W, Lopez A, Keniry M, and Gilkerson R, Oxidative insults disrupt OPA1-mediated mitochondrial dynamics in cultured mammalian cells. Redox Rep, 2018. 23(1): p. 160–167. [PubMed: 29961397]
34. Branco AF, Pereira SP, Gonzalez S, Gusev O, Rizvanov AA, and Oliveira PJ, Gene Expression Profiling of H9c2 Myoblast Differentiation towards a Cardiac-Like Phenotype. PLoS One, 2015. 10(6): p. e0129303. [PubMed: 26121149]
35. Branco AF, Pereira SL, Moreira AC, Holy J, Sardao VA, and Oliveira PJ, Isoproterenol cytotoxicity is dependent on the differentiation state of the cardiomyoblast H9c2 cell line. Cardiovasc Toxicol, 2011. 11(3): p. 191–203. [PubMed: 21455642]
36. Tobacyk J and MacMillan-Crow LA, Fluorescence-Based Assay For Measuring OMA1 Activity. Methods Mol Biol, 2021. 2276: p. 325–332. [PubMed: 34060052]
37. Bulkley D, Innis CA, Blaha G, and Steitz TA, Revisiting the structures of several antibiotics bound to the bacterial ribosome. Proc Natl Acad Sci U S A, 2010. 107(40): p. 17158–63. [PubMed: 20876130]

38. Richter U, Ng KY, Suomi F, Marttinen P, Turunen T, Jackson C, et al. , Mitochondrial stress response triggered by defects in protein synthesis quality control. Life Sci Alliance, 2019. 2(1).
39. Richter U, Lahtinen T, Marttinen P, Suomi F, and Battersby BJ, Quality control of mitochondrial protein synthesis is required for membrane integrity and cell fitness. J Cell Biol, 2015. 211(2): p. 373–89. [PubMed: 26504172]
40. Merkwirth C, Dargazanli S, Tatsuta T, Geimer S, Lower B, Wunderlich FT, et al. , Prohibitins control cell proliferation and apoptosis by regulating OPA1-dependent cristae morphogenesis in mitochondria. Genes Dev, 2008. 22(4): p. 476–88. [PubMed: 18281461]
41. Baechler BL, Bloemberg D, and Quadrilatero J, Mitophagy regulates mitochondrial network signaling, oxidative stress, and apoptosis during myoblast differentiation. Autophagy, 2019. 15(9): p. 1606–1619. [PubMed: 30859901]
42. Patten DA, Wong J, Khacho M, Soubannier V, Mailloux RJ, Pilon-Larose K, et al. , OPA1-dependent cristae modulation is essential for cellular adaptation to metabolic demand. EMBO J, 2014. 33(22): p. 2676–91. [PubMed: 25298396]
43. Yang J, Liu X, Bhalla K, Kim CN, Ibrado AM, Cai J, et al. , Prevention of apoptosis by Bcl-2: release of cytochrome c from mitochondria blocked. Science, 1997. 275(5303): p. 1129–32. [PubMed: 9027314]
44. Ellerby HM, Martin SJ, Ellerby LM, Naiem SS, Rabizadeh S, Salvesen GS, et al. , Establishment of a cell-free system of neuronal apoptosis: comparison of premitochondrial, mitochondrial, and postmitochondrial phases. J Neurosci, 1997. 17(16): p. 6165–78. [PubMed: 9236228]
45. Hedberg KK, Birrell GB, Habliston DL, and Griffith OH, Staurosporine induces dissolution of microfilament bundles by a protein kinase C-independent pathway. Exp Cell Res, 1990. 188(2): p. 199–208. [PubMed: 2185942]
46. Sin J, Andres AM, Taylor DJ, Weston T, Hiraumi Y, Stotland A, et al. , Mitophagy is required for mitochondrial biogenesis and myogenic differentiation of C2C12 myoblasts. Autophagy, 2016. 12(2): p. 369–80. [PubMed: 26566717]
47. Bohovych I, Dietz JV, Swenson S, Zahayko N, and Khalimonchuk O, Redox Regulation of the Mitochondrial Quality Control Protease Oma1. Antioxid Redox Signal, 2019. 31(6): p. 429–443. [PubMed: 31044600]
48. Subramanian K, Jochem A, Le Vasseur M, Lewis S, Paulson BR, Reddy TR, et al. , Coenzyme Q biosynthetic proteins assemble in a substrate-dependent manner into domains at ER-mitochondria contacts. J Cell Biol, 2019. 218(4): p. 1353–1369. [PubMed: 30674579]
49. Stoldt S, Wenzel D, Kehrein K, Riedel D, Ott M, and Jakobs S, Spatial orchestration of mitochondrial translation and OXPHOS complex assembly. Nat Cell Biol, 2018. 20(5): p. 528–534. [PubMed: 29662179]
50. Gold VA, Brandt T, Cavellini L, Cohen MM, Ieva R, and van der Laan M, Analysis of Mitochondrial Membrane Protein Complexes by Electron Cryo-tomography. Methods Mol Biol, 2017. 1567: p. 315–336. [PubMed: 28276027]
51. Kornmann B, Currie E, Collins SR, Schuldiner M, Nunnari J, Weissman JS, et al. , An ER-mitochondria tethering complex revealed by a synthetic biology screen. Science, 2009. 325(5939): p. 477–81. [PubMed: 19556461]
52. Cipolat S, Rudka T, Hartmann D, Costa V, Serneels L, Craessaerts K, et al. , Mitochondrial rhomboid PARL regulates cytochrome c release during apoptosis via OPA1-dependent cristae remodeling. Cell, 2006. 126(1): p. 163–75. [PubMed: 16839884]
53. Senos Demarco R, Uyemura BS, D'Alterio C, and Jones DL, Mitochondrial fusion regulates lipid homeostasis and stem cell maintenance in the Drosophila testis. Nat Cell Biol, 2019. 21(6): p. 710–720. [PubMed: 31160709]

Highlights

- Mitochondrial optic atrophy-1 (OPA1) adapts mitochondrial structure to bioenergetic function: long (L-OPA1) isoforms mediate organellar fusion, but when transmembrane potential ($\Delta\Psi_m$) is lost, L-OPA1 is cleaved to short, inactive S-OPA1.
- L-OPA1 of H9c2, L6.C11, and C2C12 myoblasts are insensitive to loss of $\Delta\Psi_m$, but OPA1 processing is restored following differentiation.
- *OPA1* knockdown indicates that intact OPA1 is necessary for effective myoblast differentiation.
- OMA1-mediated OPA1 processing is a key mechanism of mitochondrial stress sensing, and is necessary for myoblast differentiation.

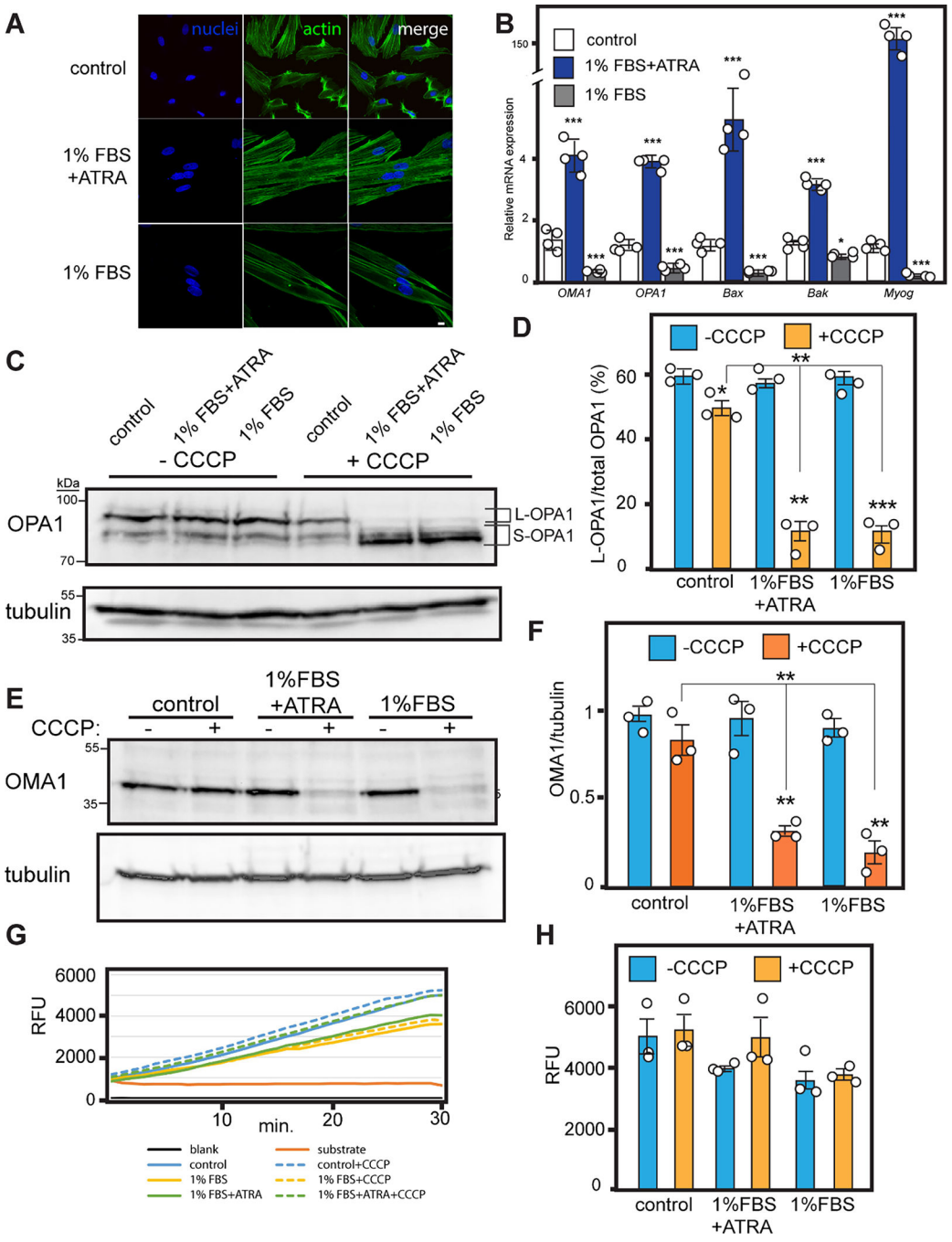

Figure 1. Differentiation activates $\Delta\Psi_m$-sensitive OPA1 processing.

A. Confocal microscopy of H9c2s grown in standard media (10% FBS) or differentiated for 5 d. in low serum with (1% FBS+ATRA) or without (1% FBS) retinoic acid. Nuclei (blue) labeled with DAPI, actin visualized with phalloidin (green). n=3 experiments. Size bar = 10 μm. **B.** Undifferentiated control and differentiated (1% FBS+ATRA or 1% FBS) H9c2s were analyzed for gene expression via qRT-PCR of the indicated mRNAs. n=4 experiments, ± SE. Student's t-test. * denotes $p<0.05$, *** denotes $p<0.001$ compared with control. **C.** Anti-OPA1 immunoblotting of undifferentiated and differentiated H9c2s without or with

CCCP challenge (10 μM, 1 hr.), with anti-tubulin loading control, bottom. n=3 independent biological replicates. **D**. ImageJ quantification of OPA1 isoforms of immunoblots in **C**, ± SE. One-way ANOVA followed by Tukey's HSD. * denotes $p<0.05$, ** denotes $p<0.01$, *** denotes $p<0.001$ compared with undifferentiated H9c2s. **E.** OMA1 immunoblotting of control and differentiated H9c2s without or with CCCP challenge (10 μM, 4 hrs.). n=3 independent biological replicates. **F.** ImageJ quantification of immunoblots in **E**, ± SE. One-way ANOVA followed by Tukey's HSD. ** denotes $p<0.01$. **G.** OMA1 functional activity assay. Lines represent the tracing as an average (n=3) over the 30 min assay reported as relative fluorescence units (RFU) excitation/emission of 325/392 nm. **H.** Histogram of activity assay in **G**. Student's t-test.

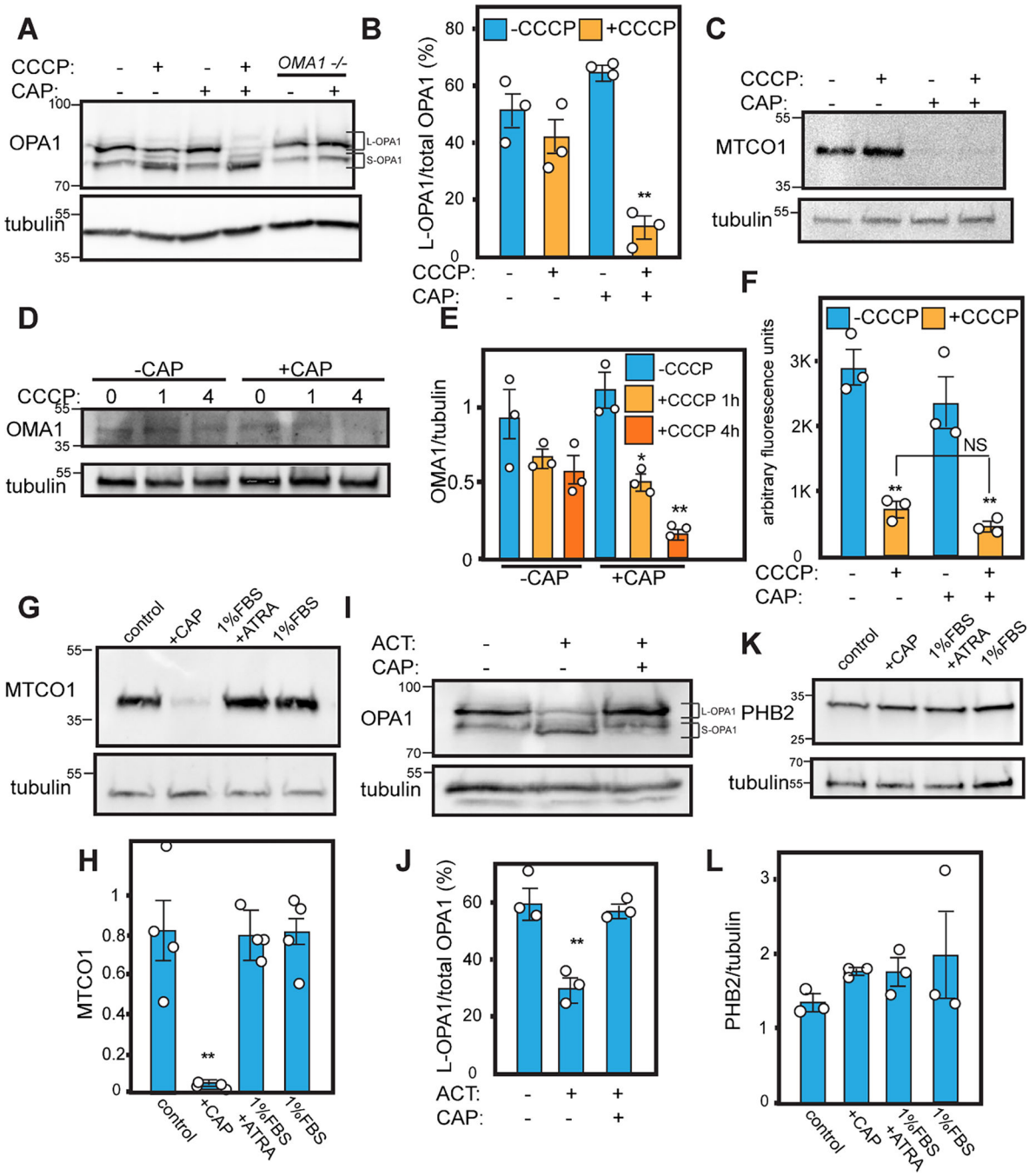

Figure 2. Inhibition of mitochondrial protein synthesis activates $\Delta\Psi_m$-sensitive OPA1 processing in undifferentiated H9c2s.

A. OPA1 immunoblotting of H9c2s grown without or with CAP (40 μg/mL) for 72 hrs. followed by CCCP challenge (10 μM, 1 hr.), as well as *OMA1*−/− MEFs. n=3 independent biological replicates. Tubulin loading control. **B.** ImageJ quantification of OPA1 isoforms in **A**. One-way ANOVA followed by Tukey's HSD. ** denotes p<0.01. **C**. Immunoblotting for mtDNA-encoded MTCO1 in lysates of **A**, above. Tubulin loading control. n=3. **D.** OMA1 immunoblotting of lysates from H9c2s grown without or with

CAP, followed by CCCP challenge for 0, 1, or 4 hrs. (10 μM), n=3 independent biological replicates. **E.** Quantification of OMA1 in **D.** One-way ANOVA followed by Tukey's HSD. * denotes $p<0.05$, ** denotes $p<0.01$. **F.** TMRE flow cytometry of H9c2s without or with CAP followed by CCCP challenge, each data point represents mean fluorescence of 10,000 events. n=3 experiments, ± SE. ** denotes $p<0.01$. **G**. MTCO1 immunoblotting of control, CAP-treated, and differentiated (1% FBS+ATRA, 1% FBS) H9c2s. Tubulin loading control. n=3 independent biological replicates. **H**. Quantification of MTCO1 in **G. I.** OPA1 immunoblotting of H9c2s treated with ACT (150 mM, 24 hrs.), CAP (40 mg/mL, 72 hrs.) or both. **J**. ImageJ quantification of OPA1 isoforms in **I**. **K.** PHB2 immunoblotting of control, CAP-treated, and differentiated (1% FBS+ATRA, 1% FBS) H9c2s. Tubulin loading control. **L**. ImageJ quantification of PHB2 blotting in **K**. All immunoblot quantifications analyzed by one-way ANOVA with Tukey's HSD, ± SE. * denotes $p<0.05$, ** denotes $p<0.01$.

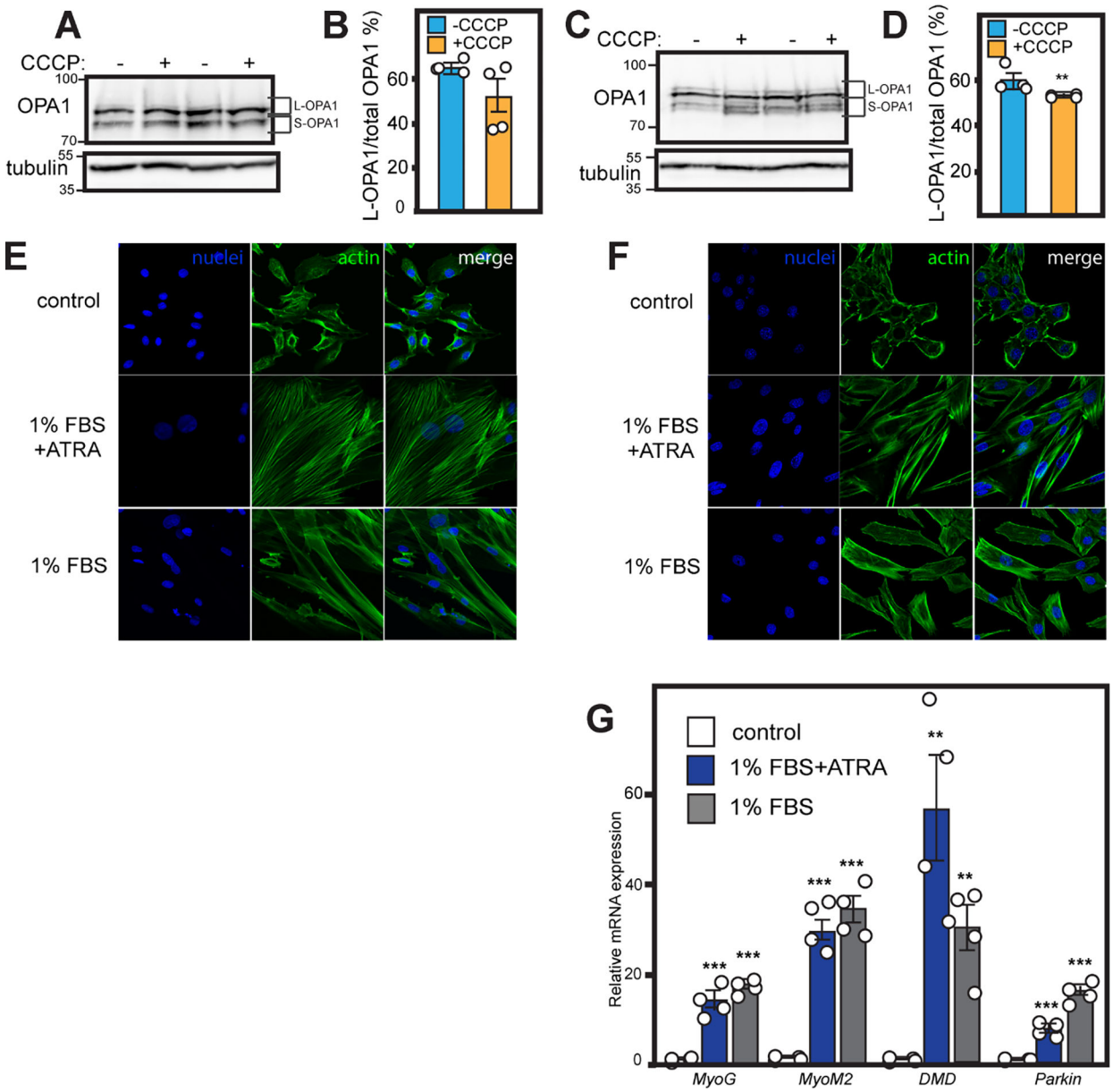

Figure 3. L6C11 and C2C12 myoblasts undergo differentiation.

A. OPA1 immunoblotting of L6.C11 myoblasts without or with CCCP challenge (10 μM, 1 hr.). Two independent biological replicates shown. Tubulin loading control. n=4 expts. **B**. ImageJ quantification of OPA1 isoforms in **A**. **C.** OPA1 immunoblotting of C2C12 myoblasts without or with CCCP challenge (10 μM, 1 hr.). Two independent biological replicates shown. n=3 expts. Tubulin loading control. **D**. ImageJ quantification of OPA1 isoforms in **C**. **E.** Confocal imaging of undifferentiated (control) and differentiated (1% FBS+ATRA, 1% FBS) L6.C11s. Nuclei were imaged with DAPI (blue) and actin visualized with phalloidin (green). Size bar = 10 μm. **F.** Confocal imaging of undifferentiated (control) and differentiated (1% FBS+ATRA, 1% FBS) C2C12s as in **C**. Size bar = 10 μm.

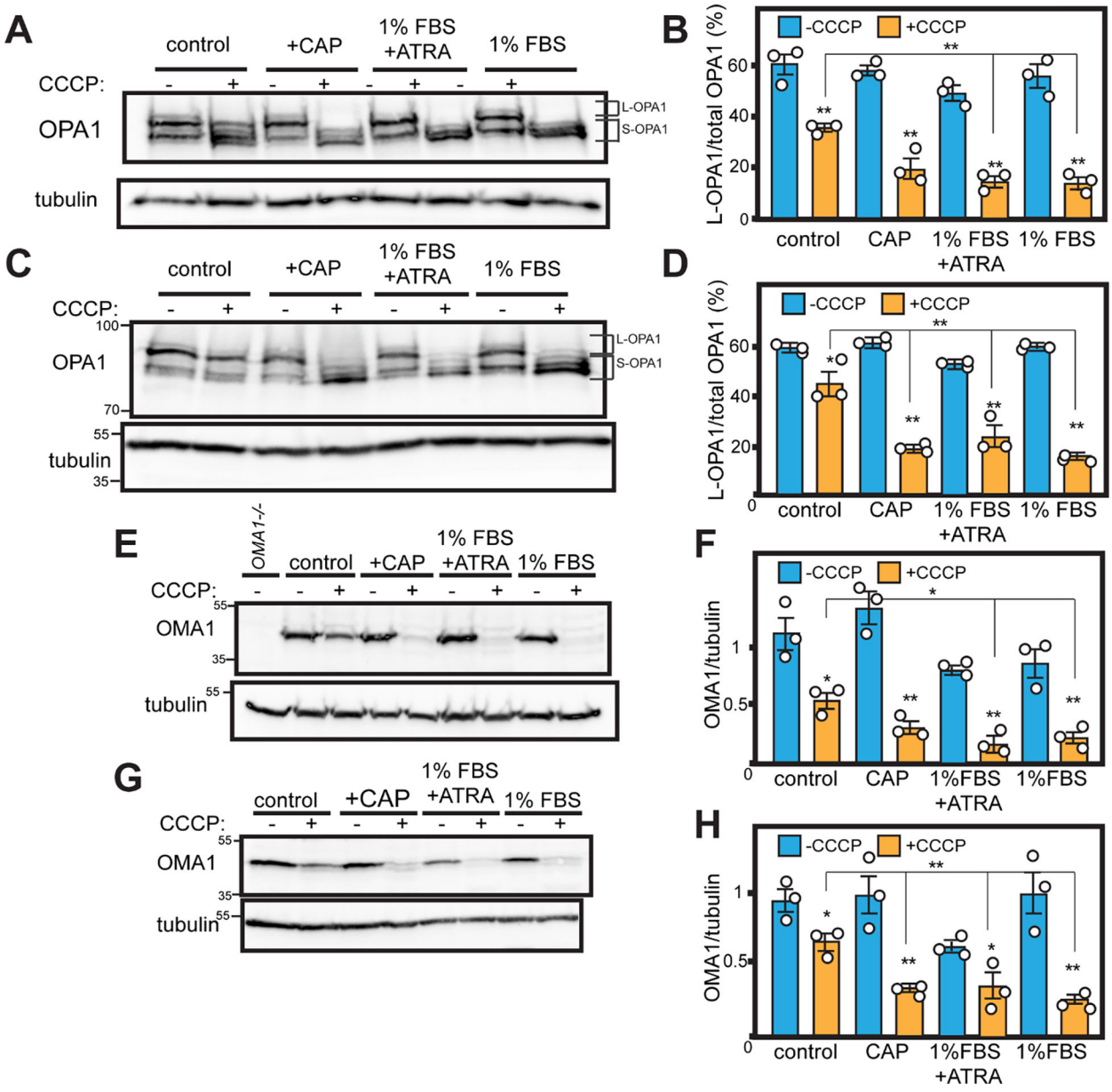

Figure 4. L6.C11 and C2C12 myoblasts engage $\Delta\Psi_m$-sensitive OPA1 processing upon differentiation or inhibition of mitochondrial protein synthesis.

A. OPA1 immunoblotting of control, CAP-treated, and differentiated (1% FBS+ATRA, 1% FBS) L6.C11s without or with CCCP challenge (10 μM, 1 hr.). n=3 biological replicates. **B.** ImageJ quantification of OPA1 isoforms in **A**. **C.** OPA1 immunoblotting of control, CAP-treated, and differentiated (1% FBS+ATRA, 1% FBS) C2C12s without or with CCCP challenge (10 μM, 1 hr.). n=3 biological replicates. **D.** ImageJ quantification of OPA1 isoforms in **C**. **E**. OMA1 immunoblotting of L6.C11 myoblasts without and with 10 μM CCCP challenge (4 hr.) and *OMA1*−/− MEFs. Tubulin loading control. n=3. **F**. ImageJ quantification of OMA1 in **E**. **G**. OMA1 immunoblotting of C2C12 myoblasts as in **E**. n=3. **H**. ImageJ quantification of OMA1 in **G**. All immunoblot quantifications analyzed by one-way ANOVA with Tukey's HSD, ± SE. * denotes $p<0.05$, ** denotes $p<0.01$.

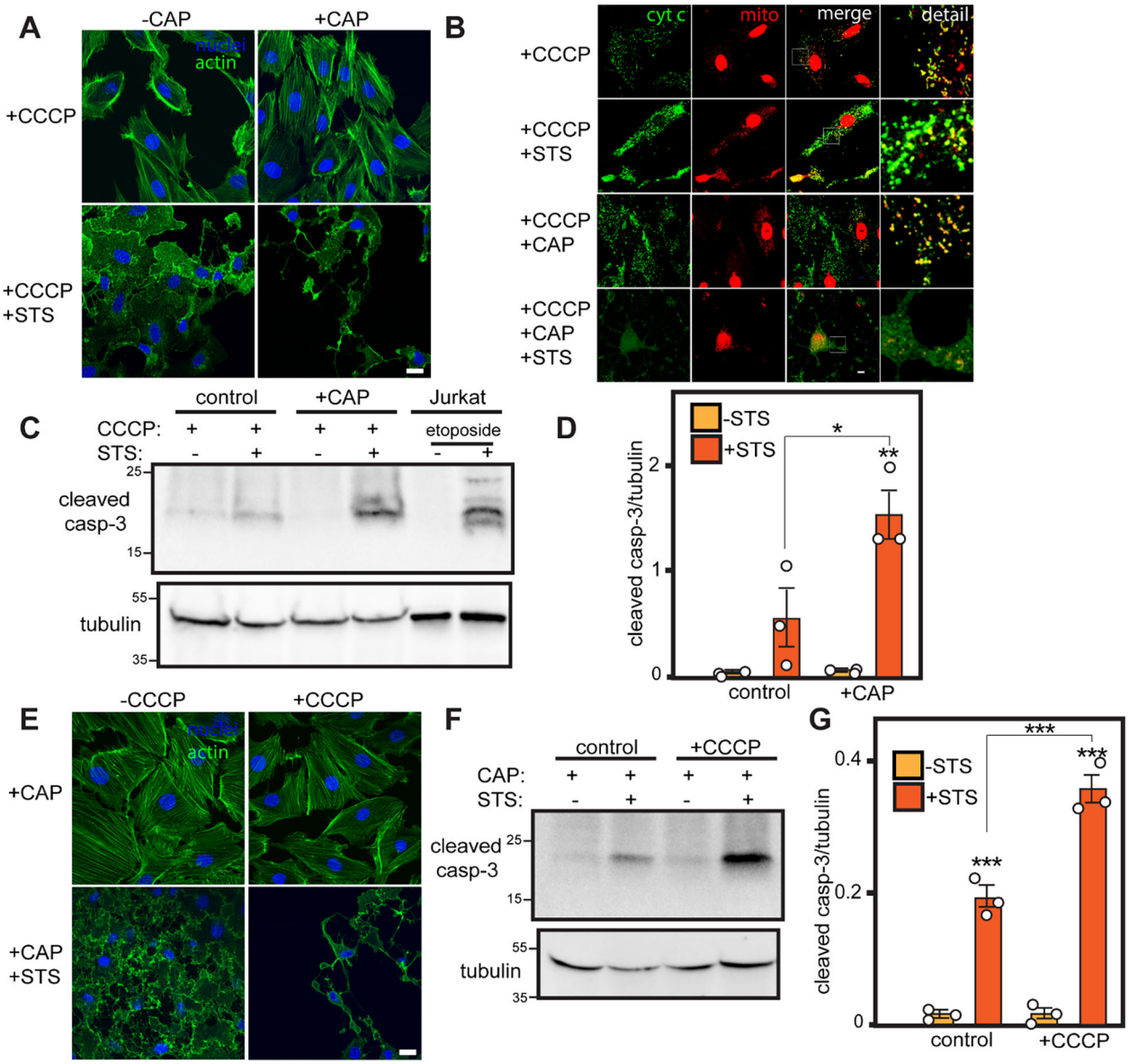

Figure 5. CAP-treated H9c2s show increased sensitivity to staurosporine-induced apoptosis.

A. Confocal imaging of H9c2s without or with CAP and staurosporine (STS) (1 μM, 2 hrs.) in the presence of 10 μM CCCP. Actin cytoskeleton visualized with phalloidin (green), cell nuclei visualized with DAPI (blue). Size bar = 20 μm. n=3 biological replicates. **B**. Confocal imaging of H9c2s, with treatments as in **A**, for nuclei (DAPI, cyan), cytochrome c immunolabeling (green), and mitochondria (mCherry-mito-7, red). n=3 expts. Size bar = 10 μm. **C.** Cleaved caspase-3 immunoblotting of H9c2s without or with CAP and staurosporine (STS) (1 μM, 2 hrs.) in the presence of 10 μM CCCP. Jurkat cell control lysates without or with etoposide. Tubulin loading control. n=3 biological replicates. **D.** ImageJ quantitation of cleaved caspase-3 immunoblotting. One-way ANOVA with Tukey's HSD, ± SE. * denotes $p<0.05$, ** denotes $p<0.01$. **E**. Confocal imaging of H9c2s without or with CCCP and STS (1 μM, 2 hrs.) in the presence of CAP. Actin cytoskeleton visualized with phalloidin (green), cell nuclei visualized with DAPI (blue). Size bar = 20 μm. n=3

biological replicates. **F**. Cleaved caspase-3 immunoblotting of H9c2s without or with 10 μM CCCP and staurosporine (STS) (1 μM, 2 hrs.) in the presence of CAP. Tubulin loading control. n=3 biological replicates. **G.** ImageJ quantification of cleaved caspase-3 immunoblotting. One-way ANOVA with Tukey's HSD, ± SE. * denotes $p<0.05$, ** denotes $p<0.01$.

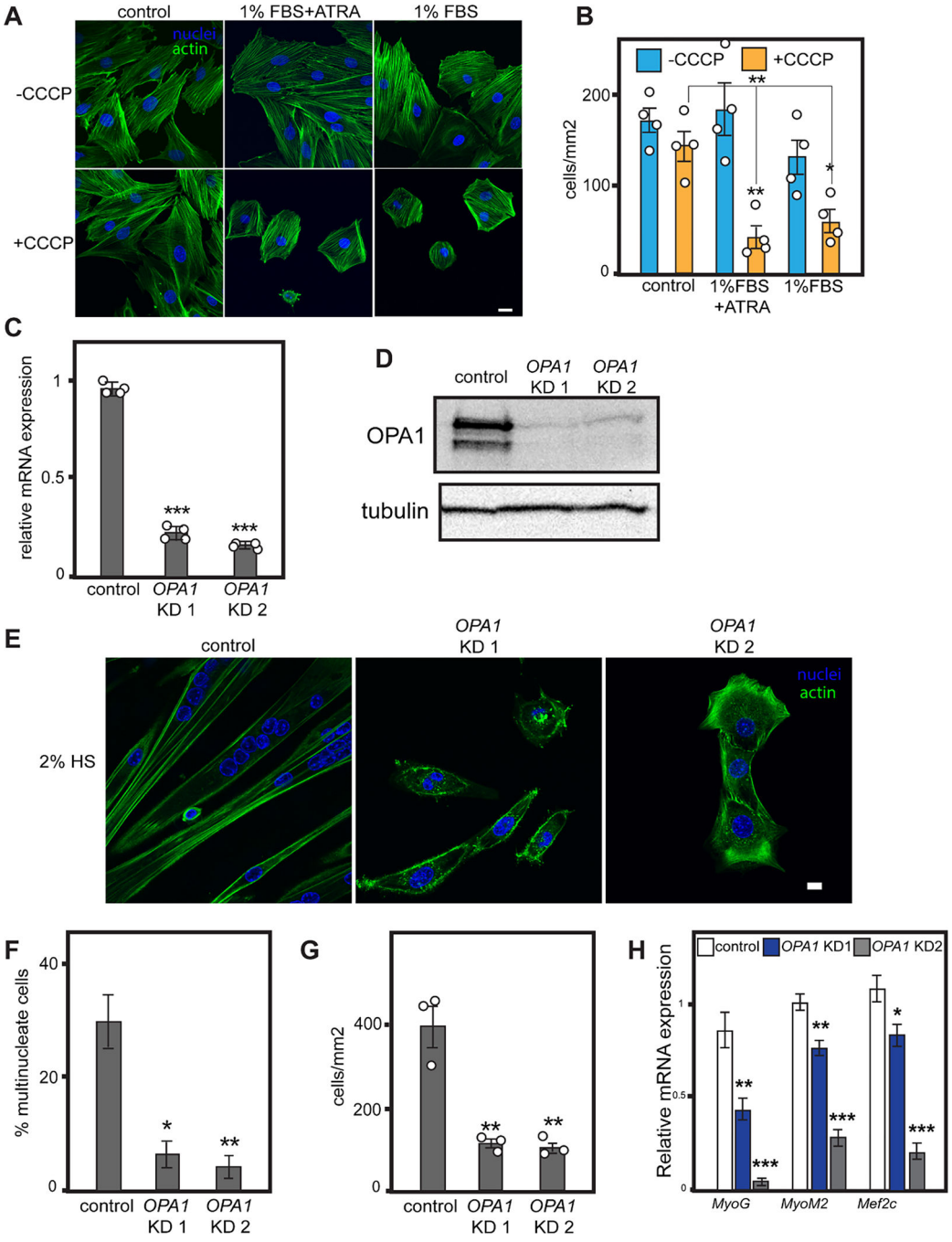

Figure 6. Loss of L-OPA1 disrupts differentiation in myoblasts.

A. H9c2s were seeded to coverslips overnight followed by growth in standard media with 10% FBS (control) or differentiated (1% FBS+ATRA or 1% FBS) for 24 hr. without or with 10 μM CCCP. Cells imaged for nuclei (DAPI, cyan) and actin (phalloidin-Alexa488, green). Size bar = 10 μm. n=4 independent biological replicates. **B**. Cell density (cells/mm^2) of H9c2s in **A**, quantitated from confocal microscopy. Student's t-test, ± SE. * denotes p<0.05, ** denotes p<0.01. **C**. mRNA levels of OPA1 in control and *OPA1* KD C2C12s (1 and 2) samples. n=4 expts. Student's t-test, ± SE, *** denotes p<0.001. **D**. OPA1

immunoblotting of control and *OPA1* KD C2c12s. Tubulin loading control. n=3 expts. **E**. Confocal microscopy of control and OPA1 KD C2C12s differentiated in media with 2% HS for 6d. Actin (green, phalloidin) and nuclei (blue DAPI). Size bar = 10 μM. n=3 expts. **F**. Quantitation of multinucleate cells in **E**. n=3. ±SE. **G**. Cell density (cells/mm^2) of C2C12s in **E**, quantitated from confocal microscopy. Student's t-test, ± SE. ** denotes p<0.01. **H**. qRT-PCR of myogenic mRNAs in control and *OPA1* KD C2C12s differentiated with 2% HS. n=4. ±SE. For all, * p<0.05, ** p<0.01, *** p<0.001.